Research Square

Preprints are preliminary reports that have not undergone peer review.
They should not be considered conclusive, used to inform clinical practice,
or referenced by the media as validated information.

Heterojunction Engineering for Boosted Interfacial Charge Separation: Intimate Face-to-Face 2D/2D SnWO4/BiOBr Z-Scheme Heterojunction for Photocatalytic Remediation

Bin Dong
Xinxiang University
Liangliang Chu
chuliangliang@xxu.edu.cn

Xinxiang University
Han Dai
Xinxiang University
Yanbo Wang
Xinxiang University
Xiaoyu Wang
Xinxiang University
Jianwei Zhou
Xinxiang University
Chubei Wang
Xinxiang University
Fangfang Duo
Xinxiang University
Shihan Wang
Xinxiang University
Zhangying Cheng
Xinxiang University

Research Article

Keywords: SnWO4, BiOBr, 2D/2D heterojunction, Z-scheme, Photocatalysis, Organic pollutant degradation

Posted Date: November 12th, 2026

DOI: https://doi.org/10.21203/rs.3.rs-11516938/v1

License: This work is licensed under a Creative Commons Attribution 4.0 International License.
Read Full License

Additional Declarations: No competing interests reported.

Heterojunction Engineering for Boosted Interfacial Charge Separation: Intimate Face-to-Face 2D/2D $SnWO_4$/BiOBr Z-Scheme Heterojunction for Photocatalytic Remediation

Bin Dong[b], Liangliang Chu[a,b,c*], Han Dai[b], Yanbo Wang[a], Xiaoyu Wang[a], Jianwei Zhou[b], Chubei Wang[a,b], Fangfang Duo[a,b], Shihan Wang[b], Zhangying Cheng[b]

[a] *Henan Photoelectrocatalytic Material and Micro-nano Application Technology Academician Workstation, Xinxiang University, Xinxiang, Henan 453003, PR China*

[b] *School of Chemistry & Materials Engineering, Xinxiang University, Xinxiang, Henan 453003, PR China*

c Huacai Lubrication Technology (Henan) Co., Ltd. Zhengzhou 453003, PR China

[*]Corresponding author.E-mail address:chuliangliang@xxu.edu.cn.

ABSTRACT: Constructing 2D/2D heterojunction is an effective strategy to suppress the recombination of photogenerated carriers and boost the photocatalytic performance of semiconductor photocatalysts. In this study, a 2D/2D direct Z-scheme $SnWO_4$/BiOBr (SWO/BOB) heterojunction photocatalyst was successfully fabricated through a facile hydrothermal route. Intimate face-to-face interfacial contact between $SnWO_4$ nanosheets and BiOBr nanoplates was verified by multiple characterizations.The as-prepared SWO/BOB composite heterojunction photocatalysts exhibited enhanced photocatalytic activity over bare $SnWO_4$ and BiOBr. The optimized 50SWO/BOB sample presented the highest degradation performance. Its RhB degradation efficiency within 25 min was 2.41 and 2.95 times that of pure SnWO4 and BiOBr, respectively, while its CIP degradation efficiency in 60 min was 3.44 times and 1.27 times higher than $SnWO_4$ and BiOBr. The improved photocatalytic performance is mainly attributed to the unique structural advantages of the 2D/2D heterostructure, which broadens the light response range and accelerates interfacial charge transfer. Radical trapping tests confirmed that h^+ was the primary reactive species, and $\cdot O_2^-$ acted as a secondary active species in the photocatalytic pollutant degradation process of the 2D/2D heterostructure. A direct Z-scheme charge transfer mechanism was proposed based on band structure analysis and existing active species. This work provides a facile strategy for the design of high-efficiency bismuth-based 2D/2D photocatalysts and theoretical support for the remediation of refractory organic wastewater.

KEYWORDS: $SnWO_4$; BiOBr; 2D/2D heterojunction; Z-scheme; Photocatalysis; Organic pollutant degradation

1. **Introduction**

Fast industrial development has led textile and pharmaceutical manufacturing effluents to discharge abundant recalcitrant organic contaminants, such as rhodamine B (RhB) and ciprofloxacin (CIP). Such persistent pollutants accumulate within food chains, posing severe risks to aquatic ecological systems and human bodies, and are difficult to eliminate via traditional water purification techniques. As an advanced oxidation technology, photocatalysis offers a viable solar-powered approach for environmental water remediation. Developing visible-light-responsive semiconductors with high charge-carrier separation efficiency is therefore highly desirable[1,2][3].

Metal tungstates have been intensively investigated for their broad application prospects in photocatalysis, optical instruments and sensor systems[4]. As a typical metal tungstate photocatalyst, α-$SnWO_4$ possesses multiple superior properties for photocatalytic reactions. Its narrow band gap enables effective visible-light absorption, while the matched band-edge position satisfies the thermodynamic requirements of redox reactions. Furthermore, the coupling effect between Sn^{2+} and W^{6+} endows the material with distinctive electron transmission capability[5].

This material can be engineered into various nanostructured morphologies through facile hydrothermal synthesis methods, which supports structural modification and heterojunction fabrication for practical photocatalytic utilization[6]. Even so, inherent shortcomings including limited visible-light absorption efficiency and inefficient charge separation greatly limit its photocatalytic performance[7]. The assembly of multicomponent semiconductor heterojunctions has emerged as a reliable approach to address these problems. This effective strategy boosts the migration and separation of photogenerated charges, broadens the spectral response range of light absorption, and promotes interfacial catalytic reaction kinetics[8].

Z-scheme heterojunctions stand out among diverse heterostructure architectures owing to their unique superiority in photocatalytic applications[9]. This structural model enables the spatial separation and transmission of photogenerated charges between different semiconductors, while retaining the powerful redox properties of the two composite components. Such structural merits efficiently inhibit the recombination of electrons and holes, promote charge segregation, and endow materials with excellent photocatalytic capability[10-12]. In addition, the microscopic morphology of photocatalysts exerts a vital impact on their catalytic performance. Two-dimensional

nanosheet structures can expose more reactive sites and reduce the migration distance of photogenerated carriers[13,14].

As a typical layered bismuth-based semiconductor with a band gap ranging from 2.6 to 2.9 eV, bismuth oxybromide (BiOBr) has drawn extensive research interest in the field of photocatalysis. Its unique layered structure favors the migration of photogenerated charges, while pure BiOBr suffers from inherent limitations including brief carrier lifespan and high interfacial impedance[15,16]. Numerous prior investigations have verified that coupling BiOBr with functional materials such as Bi_2MoO_6[17] and NiFe-LDH[18] can effectively improve photocatalytic performance. Nevertheless, few systematic studies have focused on the $SnWO_4$/BiOBr composite photocatalytic system. Benefiting from well-matched band structures, both $SnWO_4$ and BiOBr are capable of forming nanosheet structures through hydrothermal synthesis, constructing compact 2D/2D plate-on-plate heterojunction interfaces. This distinctive structural feature optimizes the charge transmission path, which is conducive to achieving synergistic enhancement of photocatalytic performance[14,19].

In this work, $SnWO_4$/BiOBr 2D/2D Z-scheme composites were prepared by a facile hydrothermal method. The crystal structure, morphology, optical and electronic properties were systematically characterized. The visible-light-driven photocatalytic degradation behaviors of the prepared samples were assessed using RhB and CIP as target pollutants. Z-scheme charge transfer mechanism of composite materials was clarified.

2 Experimental methods

2.1 Sample Preparation

$SnWO_4$ was prepared by hydrothermal method. Specifically, 1.808 g of $SnCl_2 \cdot 2H_2O$ was dissolved in 15 mL of dilute hydrochloric acid solution (1 M) to prepare solution A; next, 2.64 g of $Na_2WO_4 \cdot 2H_2O$ and 0.3 g of CTAB were dissolved in 20 mL of deionized water to form solution B. Under vigorous stirring, solution B was added dropwise to solution A, and then the pH of the mixture was adjusted to 7.00 with 10 M NaOH solution. Following an additional 30 minutes of stirring, the resulting suspension was poured into a 100 mL stainless steel autoclave and maintained at 200℃ for 24 h. The solid precipitate was collected via filtration and rinsed repeatedly with

deionized water and absolute ethanol in sequence. The final target product was harvested after subsequent oven drying at 70℃ overnight.

Preparation of $SnWO_4$/BiOBr: 1.6 g $Bi(NO_3)_3 \cdot 5H_2O$ was dissolved in 40mL of acetic acid aqueous solution (volume ratio of acetic acid to water is 1:7), then a certain amount of $SnWO_4$ was added and stired until the solution became uniform. Next, 0.3927 g KBr was dissolved in 30 mL of DI water and added to the above $Bi(NO_3)_3 \cdot 5H_2O$ acetic acid aqueous solution.Then, the well-mixed solution was fully added into a 100 mL autoclave, sealed and kept at 160℃ for 12 hours. The collected sediment was centrifuged and washed with ethanol and DI water, and then dried overnight to obtain the final $SnWO_4$/BiOBr composite samples. For convenience's sake, composite samples with $SnWO_4$ mass fractions of 30%, 50% and 80% were denoted as 30SWO/BOB, 50SWO/BOB and 80SWO/BOB, respectively. Additionally, pure BiOBr was prepared following the same method above but without adding $SnWO_4$.

2.2 Performance evaluation

The photocatalytic degradation experiment was conducted using a photocatalytic reactor. Experiment process was as follows: firstly, 50 mL degradation solution with a concentration of 10 mg/L was added to a cylindrical reactor containing 50 mg photocatalyst. Then, place the reactor in the dark and stir to achieve adsorption desorption equilibrium between the catalyst and the solution. After that, the reaction solution was irradiated by a 500 W xenon lamp with a 420 nm cut-off filter. During the photoreaction process, 3-4 mL degradation solution was taken out at regular intervals and immediately centrifuged to detect the absorbance of the supernatant on a UV-vis spectrophotometer. The degradation rate is calculated by $(A_0-A_t)/A_0*100\%$, where A_0 is the initial absorbance of the solution and A_t is the absorbance at reaction time t. The temperature of the reaction system was controlled by an external condenser water tank.

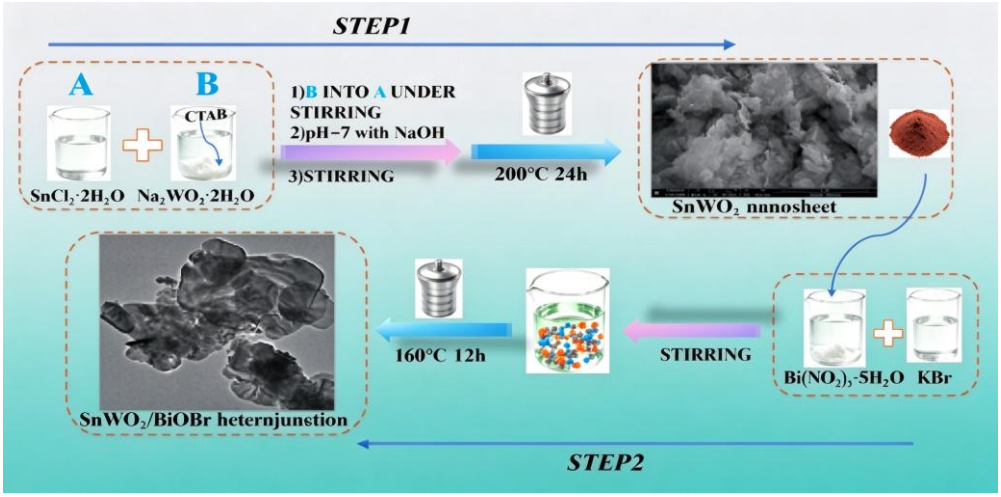
2.3 Material characterization

The crystal properties of the prepared samples were analyzed using Cu Kα radiation (K=0.15406 nm) on an X-ray diffractometer (Bruker-D8 Advance, Germany) within a 2θ range of 10° to 80° and a step size of 0.1°. Scanning electron microscope (FEI Quanta250FEG, USA) and high-resolution transmission electron microscopy (Thermo Fisher FEI Talos F200X, USA) were used to observe the surface morphology and microscopic fine structure of the sample. An X-ray photoelectron spectroscopy (Thermo Fisher Escalabxi+, USA) was adopted to analyze the elemental composition

and chemical state of the photocatalysts. An UV-visible diffuse reflectance spectrometer (Schimadzu UV-3600 Plus, Japan) was applied to examine the light absorption properties of the samples with $BaSO_4$ as the white standard. A Hitachi F-4600 spectrophotometer (Japan) was conducted to investigate photoluminescence performance of the as-prepared samples at room temperature using an excitation wavelength of 320 nm.

3 Results and Discussion

3.1 Sample characterization



Scheme 1 Schematic illustration for the fabrication of $SnWO_4$ nanosheets and 2D/2D SWO/BOB heterojunction

Scheme 1 was schematic illustration for the fabrication of $SnWO_4$ nanosheets and 2D/2D SWO/BOB heterojunction. In Step 1, $SnWO_4$ nanosheets were synthesized via a hydrothermal method using $SnCl_2{\cdot}2H_2O$ and $Na_2WO_4{\cdot}2H_2O$ as raw materials with CTAB as surfactant. The pH value of the mixed solution is adjusted to 7 by NaOH, followed by continuous stirring and hydrothermal treatment at 200° C for 24 h. In Step 2, the as-prepared $SnWO_4$ nanosheets were introduced into the precursor solution containing $Bi(NO_3)_3{\cdot}5H_2O$ and KBr. After stirring, the mixture undergone a secondary hydrothermal reaction at 160° C for 12 h to construct the 2D/2D SWO/BOB heterojunction.

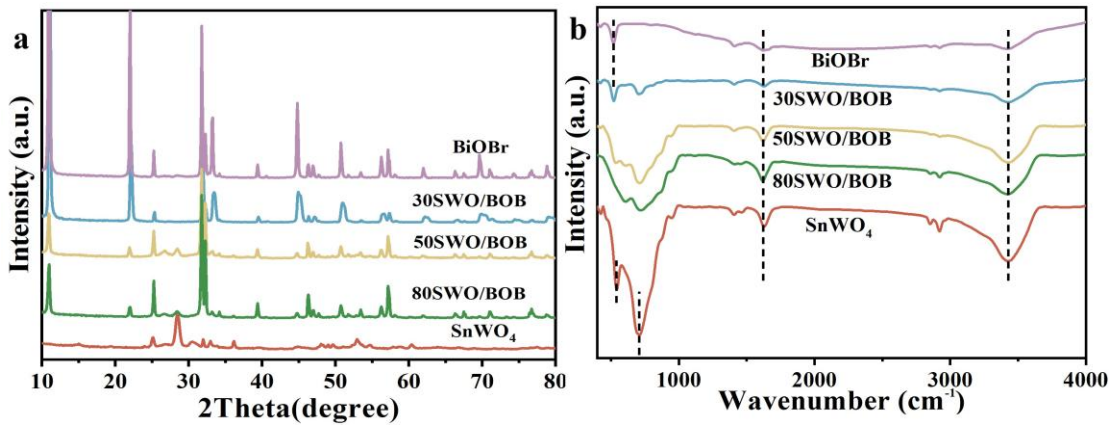


Fig. 1 XRD patterns (a) and FTIR (b) of $SnWO_4$, BiOBr and SWO/BOB composite samples

Crystal structures and phase purities of the as-prepared samples were collected by XRD measurement. Fig.1a illustrates that all diffraction signals of pristine $SnWO_4$ are highly consistent with the standard orthorhombic α-$SnWO_4$ phase (JCPDS No. 29-1354). No characteristic diffraction signals of tungsten trioxide, tin oxide or other impurities are observed, which proves the successful synthesis of high-purity α-$SnWO_4$[20]. The diffraction positions of pure BiOBr at 2θ of 10.91°、21.92°、25.20°、32.24°、 39.33°、 46.24°、 50.66° and 52.38° precisely correspond to the (001), (002), (011), (012), (112), (020) and (014) crystal planes of tetragonal BiOBr (JCPDS 02-4609)[21]. For SWO/BOB composite samples, the typical diffraction signals of BiOBr remain clearly observable. Meanwhile, the intensity of these characteristic peaks gradually declines as the $SnWO_4$ component content rises. Meanwhile, the characteristic peaks of $SnWO_4$ only appear at 25.06 ° and 28.35 ° in composite samples with a higher proportion of $SnWO_4$ (50% and 80%). And the peak intensity at 25.06 ° strengthens with the increase of $SnWO_4$ addition. XRD patterns verify the successful fabrication of SWO/BOB composite materials. FTIR spectra shown in Fig. 1b demonstrate that pure $SnWO_4$ displays characteristic absorption bands at around 560 cm^{-1} assigned to Sn-O stretching vibrations and 770 cm^{-1} originating from W-O stretching. For pristine BiOBr, a band near 520 cm^{-1} corresponds to Bi–O stretching modes. The peaks at 1655 and 3433 cm^{-1} correspond respectively to the bending and stretching vibrations of the O–H bond in water molecules. The hybridization process induces noticeable shifts and broadening in the characteristic Sn–

O, W–O, and Bi–O vibration peaks. Variations in peak intensity follow a regular trend as the loading amount of $SnWO_4$ increases. These phenomena validate the successful fabrication of SWO/BOB composites with robust interfacial coupling effects[6,12,13].

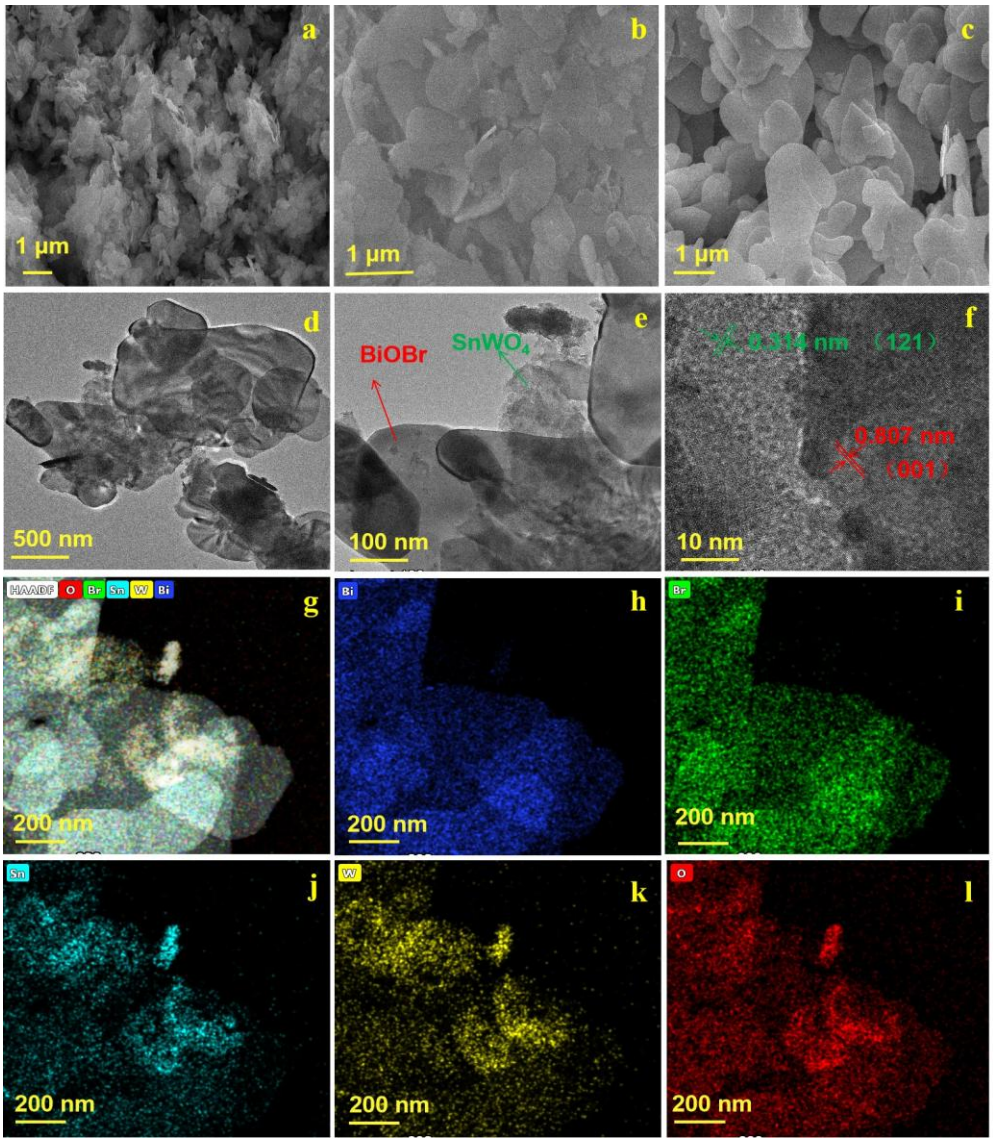


Fig.2 SEM images of $SnWO_4$ (a)、50SWO/BOB (b) and BiOBr (c); TEM image of 50SWO/BOB (d) and enlarged image of 50SWO/BOB (e); HRTEM image of 50SWO/BOB (f); EDS pattern (g) and corresponding elemental mapping photos of 50SWO/BOB (h-l)

Microstructure photographs of $SnWO_4$、50SWO/BOB and BiOBr were obtained and presented in Fig.2 (a-c). Fig. 2a reveals that pure $SnWO_4$ presents an irregular nanosheet microstructure. Pristine BiOBr exhibits smooth nanoplates with varied dimensions, as displayed in Fig. 2c. The 50SWO/BOB composite in Fig. 2b is constructed by two kinds of nanosheets with distinct sizes. Tiny $SnWO_4$ nanosheets are

randomly anchored on the surface of large-sized BiOBr nanosheets. The intimate interfacial contact between the two components facilitates electron migration and accelerates the separation of photogenerated charge carriers. Coexistence of $SnWO_4$ and BiOBr can be further verified by TEM and HRTEM analysis (Fig.2 d-f). The clear overlaps and boundaries between the layers in the TEM image demonstrate a sheet-on-sheet structure of the composite material. Lattice stripes with the lattice spacing of 0.314 nm and 0.807 nm were found (Fig.2f) which can be assigned to (121) and (001) plane of $SnWO_4$ and BiOBr, respectively[22,23].

Moreover, EDS elemental mapping show the constituent elements bismuth (Bi)、oxygen (O)、tin (Sn)、tungsten (W) and bromide (Br) all exist in the composite material and they distribute uniformly on the surface of the composite. The above result suggests the successful construction of SWO/BOB composite sample.

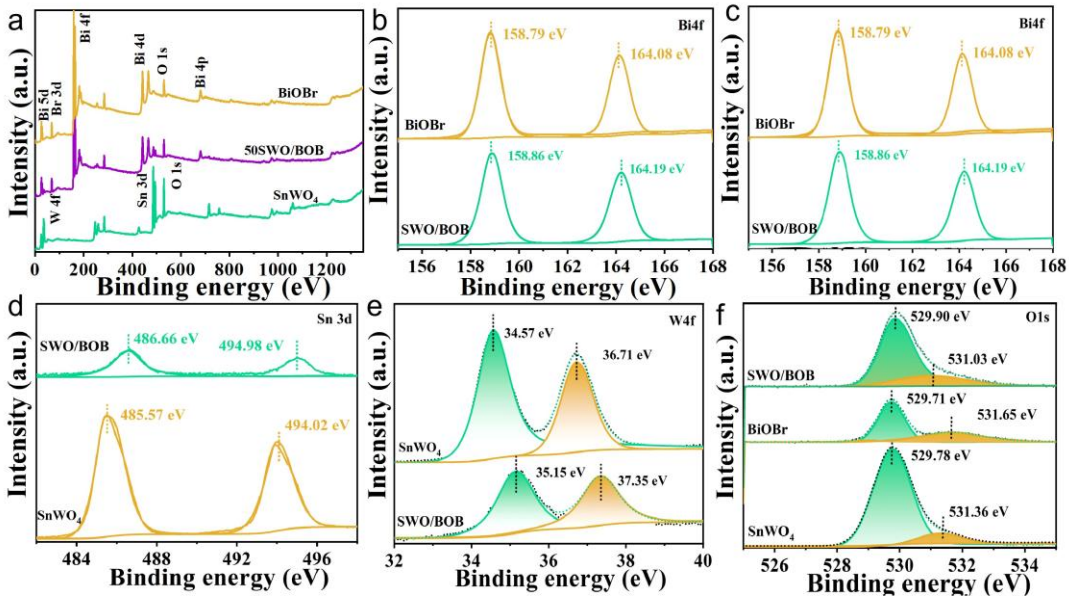


Fig. 3 Survey XPS spectras of $SnWO_4$、BiOBr and 50SWO/BOB (a); High-resolution XPS spectra of Bi (b), Br (c), Sn (d), O (e) and W (f) in corresponding samples.

XPS spectras of $SnWO_4$、BiOBr and 50SWO/BOB were surveyed to further probe the detailed elemental composition and chemical state of the samples. It is clearly evident from the survey XPS spectra (Fig.3a) that Sn, W, O and Bi, O, Br appeared separately in the spectra of $SnWO_4$ and BiOBr. While, all the above elements were the

constituent components of the binary material, which agree with the result of EDS and element mapping (Fig.2g-i). In detail, the two peaks of single BiOBr located at the binding energy of 158.79 eV and 164.08 eV were refered to as Bi^{3+} of Bi4f7/2 and Bi4f5/2 orbitals,respectively (Fig.3b)[24]. Meanwhile, two Br3d peaks picked out at 47.84 eV and 68.96 eV revealed the valence state of Br^-(Fig.3c)[25]. As shown in Fig.3d, the two XPS peaks of pure $SnWO_4$ at 485.57 eV and 494.02 eV ascribed to 3d5/2 and 3d3/2 of Sn^{2+}[26]. W4f spectra in Fig.3e also contained two typical characteristic peaks at 34.57 eV and 36.71 eV, corresponding to W^{6+}[27]. For O1s (Fig.3f) , two fitted peaks around 529 eV and 531 eV contribute to lattice oxygen (Bi-O, Sn-O) and surface hydroxyl oxygen (OH-), respectively[28].

Compared with the pure samples, the peak positions of the elements in the composite sample have shifted. For instance, peaks of Sn3d, W4f, Bi4f and Br3d all shifted to higher binding energies. The displacement of peak positions in composite materials is a common phenomenon, which can be explained by changes in electron density around the element[29,30]. Usually, a shift towards higher binding energies indicates a decrease in electron density, and vice versa. The XPS results further indicate the successful construction of composite samples[31-33].

3.2 Photocatalytic performance of as-prepared materials

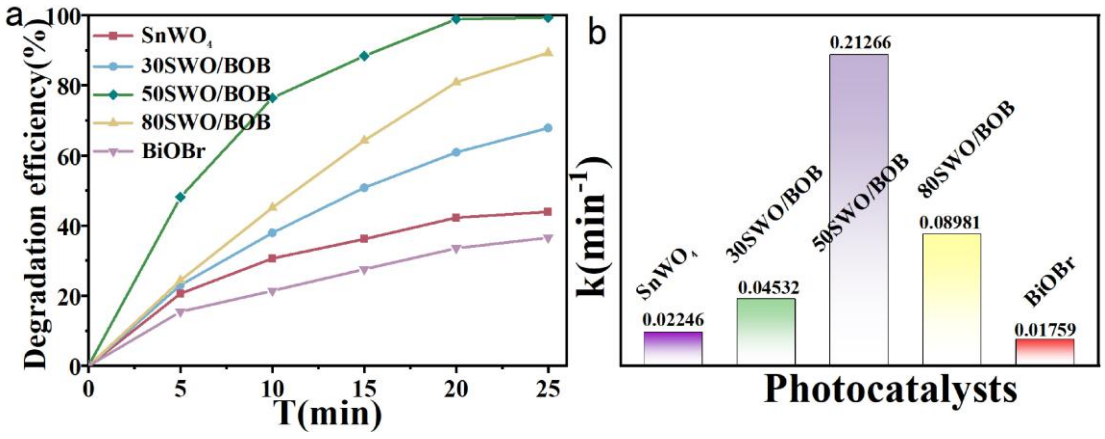


Fig. 4 Photocatalytic degradation performance of the as-prepared samples toward RhB under visible light irradiation. (a) Time-dependent degradation efficiency curves; (b) Corresponding pseudo-first-order kinetic rate constants (k). ([RhB] =10 mg/L, [catalyst] = 40 mg)

Photodegradation ability of pure $SnWO_4$、BiOBr and composite SWO/BOB was

evaluated by selecting RhB and CIP as probe pollutants. Fig.4 presents the degradation results for RhB, as shown in Fig.4a, the photocatalytic performance of composite samples is significantly improved compared with pure samples after 25min of photodegradation. The photocatalytic efficiencies of $SnWO_4$ and BiOBr were 41.25% and 33.67%, respectively, while those of 30SWO/BOB、50SWO/BOB and 80SWO/BOB were 67.82%、99.33% and 89.28% separately. To further quantify the reaction rate, the apparent rate constants (k) were calculated based on the pseudo-first-order kinetic model, and the results are summarized in Fig.4b. The 50SWO/BOB composite delivers the maximum k value of 0.21266 min^{-1}, which is approximately 9.5 times and 12.1 times higher than that of bare $SnWO_4$ (0.02246 min^{-1}) and BiOBr (0.01759 min^{-1}), respectively. Based on the above results, it can be concluded that the photodegradation performance of composite materials first increases and then decreases with the increase of SWO addition. Obviously, 50SWO/BOB was the optimal one among all samples. The results indicate that $SnWO_4$ can act as a good co-catalyst for improving the photocatalytic performance of BiOBr[34]. However, the excess $SnWO_4$ load would not only hinder the light-harvesting of BiOBr but also cover the active sites.

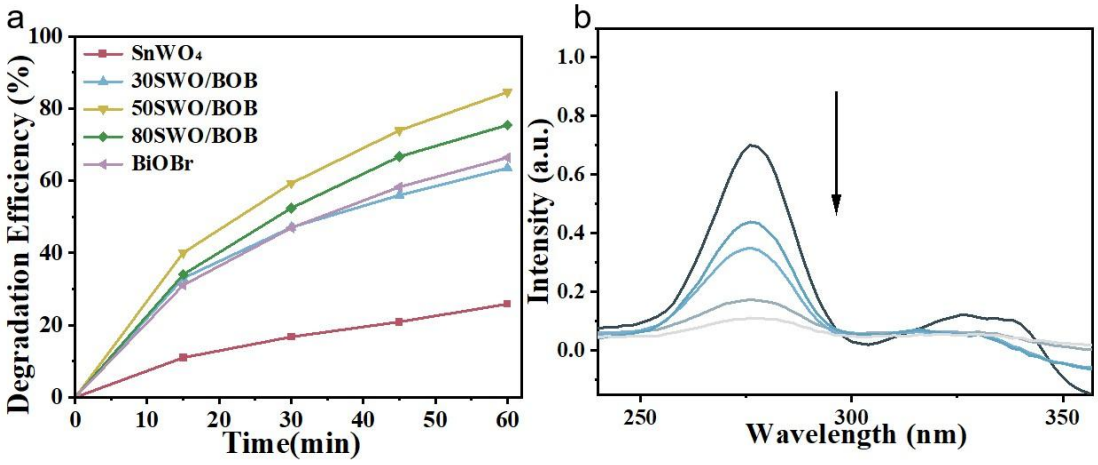


Fig. 5 Photocatalytic performance of the as-prepared materials toward CIP under visible light ([CIP] =10 mg/L, [catalyst] = 40 mg) (a); Time-dependent absorption spectra of CIP (b).

Ciprofloxacin hydrochloride serves as a clinical agent for the therapy of diverse infections triggered by susceptible bacteria, including urinary-genital, respiratory,

gastrointestinal, skin and soft tissue infections [35,36]. Improper antibiotic application represents a prevalent issue in contemporary medical systems. Such misuse may induce multiple adverse consequences, for instance the emergence of superbugs, elevated resistance among pathogenic microorganisms, environmental contamination and disrupted ecological equilibrium[35,36]. So the removal of antibiotic is particularly important. Here, CIP was selected as the model pollutants to investigate the photocatalytic performance of the as-prepared samples. Photocatalytic degradation behavior of CIP was shown in Fig.5. The photocatalytic degradation efficiency of $SnWO_4$、BiOBr and 30SWO/BOB、50SWO/BOB、80SWO/BOB at 60min were 24.64%、66.69%、63.61%、84.66% and 75.77%, respectively (Fig.5a). Obviously, the photocatalytic activity of $SnWO_4$ was enhanced when coupled with BiOBr. As the content of $SnWO_4$ in the composite material increases from 30 to 80, the photocatalytic activity first first increased and then decreased. The optimal one obtained was 50SWO/BOB. Time-dependent absorption spectra was used to further illustrate that CIP can be effectively photocatalytic degraded. Fig.5b presents time-resolved absorption spectra recorded during CIP degradation over the 50SWO/BOB sample. The gradual drop in CIP absorbance along with prolonged reaction time reveals the decrease in CIP concentration originating from photocatalytic degradation.

3.3 Possible mechanism of augmented photocatalytic activity

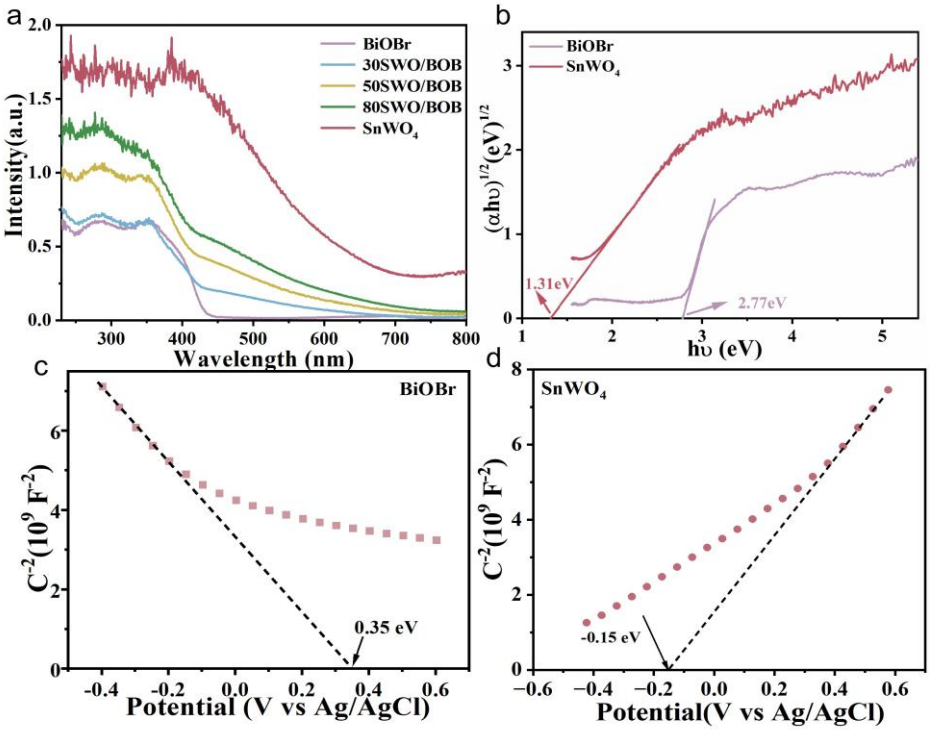


Fig. 6 UV-Vis DRS of the as-prepared samples(a), Tauc plot of $SnWO_4$ and BiOBr(b), Mott-Schottky plot of BiOBr (c) and Mott-Schottky plot of $SnWO_4$ (d).

Light absorption properties of the as-prepared samples were characterized with the UV-Vis DRS (Fig.6a). As shown in Fig.6a, all samples can absorb both ultraviolet and visible light. The absorption edge of BiOBr was 445 nm and that of $SnWO_4$ was 650 nm. Compared with BiOBr, $SnWO_4$ and the composite samples have stronger absorption intensity in the range from 200 to 800 nm. Moreover, the light absorption edge of the composite samples red shifted from 472 nm of 30SWO/BOB to 677nm of 80SWO/BOB. Tauc' equation $\alpha h\nu=A\ (h\nu-E_g)^{n/2}$ was used to calculate the band gap (E_g) of the as-prepared samples. Among which, α、h、ν、A and E_g are the optical absorption coefficient, planck constant, photon frequency, a constant and band gap, respectively[37]. For n, its value is related to the type of semiconductor (n=4 for indirect band gap semiconductors,while, for direct band gap semiconductors n=1)[38,39]. As BiOBr and $SnWO_4$ both are indirect band gap semiconductors，thus band gaps of as-prepared samples could be estimated from the plot of $(\alpha h\nu)^{1/2}$ vs hν [42,43]. Fig.6b presents the band gap (Eg) values of various samples. The measured data reveal that BiOBr and $SnWO_4$ possess band gaps of approximately 2.77 eV and 1.31 eV,

respectively. In order to determine the band structure of BiOBr and $SnWO_4$, Mott-Schottky test was conducted to estimate the conduction band (E_{CB}) of BiOBr and $SnWO_4$ (Fig.6c and d). By performing linear fitting on the obtained Mott-Schottky curves, the flat-band potentials of BiOBr and $SnWO_4$ were determined to be 0.35 and -0.15 V, respectively, relative to the Ag/AgCl reference electrode (Fig.6d)[42,43]. According to the Nernst equation: $E_{NHE}=E_{Ag/AgCl}+0.197$[46,47], the flat-band potentials of BiOBr and $SnWO_4$ were calculated as 0.547 and 0.047 V, respectively, relative to the standard hydrogen electrode. A positive slope acquired from Mott-Schottky fitting curve is characteristic of n-type semiconductors , while a negative slope indicates p-type semiconductor[46]. Consequently, BiOBr and $SnWO_4$ are p-type and n-type, respectively. Typically, the Fermi level (E_f) of n-type semiconductors is very close to the conduction band bottom (0.1-0.3 V), whereas the E_f of p-type semiconductors is near the valence band top (0.1-0.3 V)[47]. The valence band of BiOBr was found to be 0.747 V, and the conduction band of $SnWO_4$ was -0.153 V. From $Eg=Ev_B-Ec_B$, the conduction band of BiOBr is -2.023 V, and the valence band of $SnWO_4$ is 1.157 V[48]. The band structure diagrams of BiOBr and $SnWO_4$ can be determined as shown in Scheme 2.

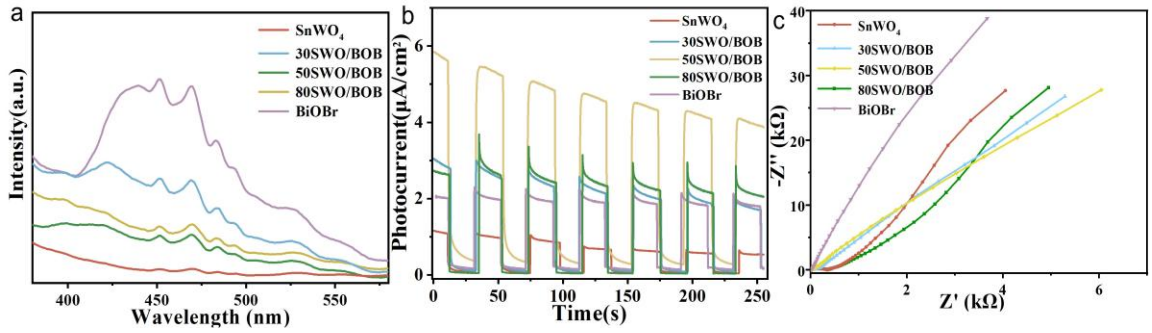


Fig. 7 PL spectra (a), Transient photocurrent response curves (b) and EIS spectra (c) of the as-prepared samples.

PL emission intensity reflects the recombination rate of photogenerated electron-hole pairs. Reduced fluorescence peak intensity means stronger restraint on charge recombination and improved separation efficiency of photogenerated carriers, which generally contributes to superior photocatalytic activity[49,50].

Fig.7a was PL spectra of the as-prepared samples (λ_{ex}=325 nm). As displayed in Fig. 7a, BiOBr presented the strongest PL emission, with its main peaks centered at 450 nm and 475 nm. In contrast, pristine $SnWO_4$ yielded the weakest fluorescence response, reflecting less pronounced intrinsic recombination relative to BiOBr. The other samples had the similar PL peaks but show fluorescence intensities between the two extremes, decreasing gradually with increasing $SnWO_4$ content: fluorescence intensity sequence: BiOBr > 30SWO/BOB > 80SWO/BOB > 50SWO/BOB > $SnWO_4$. When SWO/BOB heterojunction is established, the built-in electric field formed at the interface drives the migration of photo generated electron-hole pairs across the interfacial region, effectively hindering carrier recombination. Notably, 50SWO/BOB exhibits the optimum charge carrier separation performance in the composite samples[51].

The photocurrent density represents the number of photogenerated electrons that can migrate to the electrode surface per unit time: the higher photocurrent, the stronger the carrier migration ability.The cycling curve of the switch light shows no significant attenuation, indicating that the material has good light stability[52]. The photocurrent test results are shown in Fig. 7b, and it can be seen that the order of photocurrent intensity for different samples is: 50SWO/BOB>80SWO/BOB> 30SWO/BOB>BiOBr>$SnWO_4$. Pure SnWO has the lowest photocurrent: it has high resistance to carrier migration and poor activity when used alone; The photocurrent of pure BiOBr is higher than that of $SnWO_4$. All heterojunction composites display markedly elevated photocurrent responses relative to the two pure materials. The sample with a 50% composite ratio achieves the maximum photocurrent peak and optimal charge transfer efficiency. The heterojunction interface significantly improves the efficiency of photogenerated carrier separation and interface charge transfer; However, when the doping ratio of $SnWO_4$ is too high (80%), the photocurrent slightly decreases compared to the 50% sample. An excess of $SnWO_4$ can act as carrier recombination centers and thereby degrade the photocatalytic performance[53].

$SnWO_4$ exhibits the lowest PL fluorescence signal, indicating that the radiative recombination process of photo generated electron hole pairs is significantly suppressed, and the intrinsic separation efficiency of charge carriers is better than that

of the control sample. But the material also exhibits the weakest photocurrent response, which seems contradictory, mainly due to the high-density deep level defect traps, extremely low carrier migration rate, and high electrode interface charge transfer barrier in SWO[54,55]. The separated state carriers generated by light excitation are easily captured by lattice defects and undergo non radiative annihilation, which does not produce fluorescence at all, resulting in a significant decrease in PL intensity; However, carriers bound by defects cannot freely migrate to the electrode surface to participate in charge conduction. Furthermore, the material suffers from low inherent conductivity, accompanied by substantial scattering loss originating from grain boundaries[56,57]. Only a very small amount of photo generated charges can cross the interface barrier and enter the external circuit, resulting in the lowest photocurrent density at the macroscopic level.

The EIS test results are shown in Fig.7c. The radius of the Nyquist curve corresponds to the charge transfer impedance (Rct): the smaller radius of the arc, the lower the interface charge transfer resistance and the faster the carrier migration speed[58]. From the test results in Fig. 7c, it can be seen that the order of different sample arc radii is: BiOBr>$SnWO_4$>80SWO/BOB>30SWO/BOB>50SWO/BOB. BiOBr has the largest arc and the highest charge transfer impedance; Pure $SnWO_4$ comes second. All three heterojunction composites exhibit considerably reduced arc radii compared with the two single-component materials. Among these samples, 50SWO/BOB delivers the smallest arc size and possesses the minimum interfacial charge transfer resistance.Constructing SWO/BOB heterojunction can effectively reduce the charge transfer impedance at the solid-liquid interface and accelerate the transfer of photogenerated charges.

PL、PC and EIS measurements yield consistent results. The construction of SWO/BOB heterojunctions inhibits interfacial charge recombination, promotes charge separation efficiency and lowers the resistance for charge transport.The above experimental results can explain the photocatalytic activity of the composite sample is better than that of single BiOBr or $SnWO_4$ from the perspective of carrier dynamics.

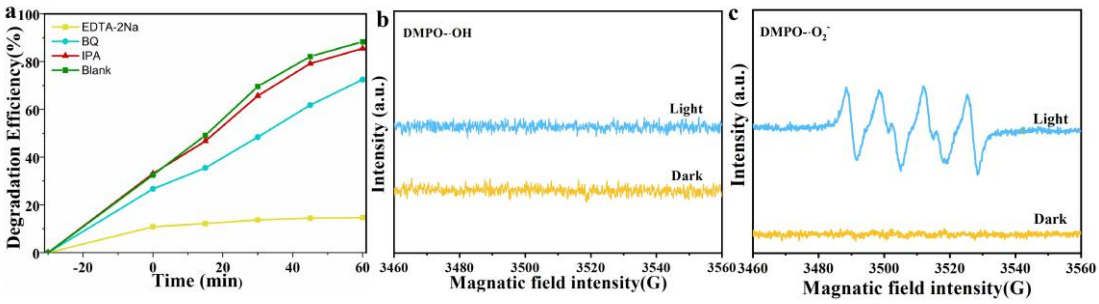
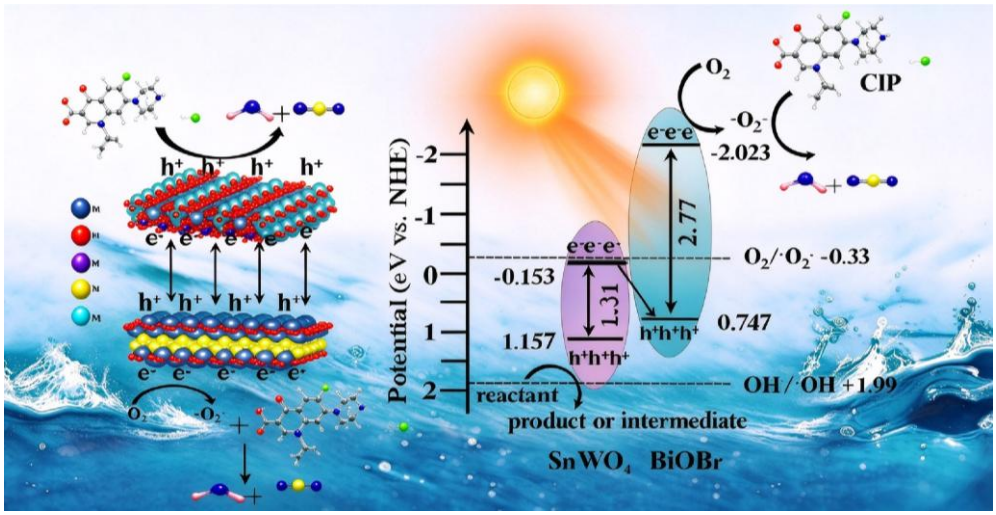


Fig. 8 Capture experiment of 50SWO/BOB under visible light irradiation (a), ESR spectra of DMPO-·OH (b) and DMPO-·O_2^- (c) over 50SWO/BOB under dark and light irradiation.

To identify the dominant reactive species involved in the photocatalytic degradation process, radical trapping experiments were carried out, where EDTA-2Na, BQ and IPA were employed as scavengers for holes (h^+), superoxide radicals (·O_2^-) and hydroxyl radicals (·OH), respectively[59]. As shown in Fig.8a, the degradation efficiency exhibited negligible variation after adding IPA compared with the blank group, demonstrating that (·OH) played a minor role in the reaction system. The addition of BQ induced a notable reduction in degradation activity, revealing that ·O_2^- represented a key reactive species. A marked decrease in degradation efficiency was detected once EDTA-2Na was added into the reaction system, demonstrating that photogenerated h^+ governed the pollutant degradation. These scavenging measurements collectively verified that photogenerated holes served as the dominant active species. ·O_2^- acted as a secondary reactive component, whereas ·OH scarcely took part in the photocatalytic degradation process.

To further verify the generation of reactive oxygen species and consolidate the above conclusion, ESR spin-trapping measurements with DMPO were performed (Fig.8b and c). In the dark environment, no obvious characteristic signals of DMPO-·O_2^- and DMPO-·OH adducts were detected. Under light irradiation, strong four-fold characteristic peaks assigned to DMPO-·O_2^- were clearly observed (Fig.8c),while negligible signal of DMPO-·OH is observed (Fig.8b). Combining the two sets of results, it can be concluded that h^+ and ·O_2^- serve as the primary reactive species for photocatalytic degradation.



Scheme 2 Photocatalytic degradation pathway of Z-scheme $SnWO_4$/BiOBr heterojunction

Scheme 2 illustrates a direct Z-scheme $SnWO_4$/BiOBr heterojunction photocatalytic system under solar irradiation, and the charge transfer and degradation mechanism is elaborated as follows: upon solar light excitation, both $SnWO_4$ and BiOBr absorb photons to generate electron-hole pairs. For $SnWO_4$, the conduction band (CB) potential is -0.153 eV vs. NHE, the valence band (VB) potential is 1.157 eV vs. NHE, with a bandgap of 1.31 eV. For BiOBr, the CB and VB potentials are -2.023 eV vs. NHE and 0.747 eV vs. NHE, respectively, and the bandgap is 2.77 eV.

Following the typical Z-scheme charge transfer pathway: photogenerated electrons on the CB of $SnWO_4$ recombine with photogenerated holes on the VB of BiOBr at the heterojunction interface. This recombination effectively eliminates carriers with weak redox capacity, while preserving highly reductive electrons on the CB of BiOBr (E_{CB}=-2.023 eV vs. NHE) and highly oxidative holes on the VB of $SnWO_4$ (E_{VB}=1.157 eV vs. NHE).

The standard redox potential of $O_2/\cdot O_2^-$ is -0.33 eV vs. NHE[60]. The CB potential of BiOBr (-2.023 eV) is more negative than this threshold, so its retained electrons can thermodynamically reduce dissolved O_2 to produce superoxide radicals $\cdot O_2^-$. The VB potential of $SnWO_4$ (1.157 eV) is lower than the potential of $OH^-/\cdot OH$) (+1.99 eV vs. NHE)[61], meaning the retained holes cannot oxidize OH^- to ·OH. The photocatalytic degradation process includes the following steps: one is that the enriched electrons on

BiOBr CB activate molecular oxygen to form $\cdot O_2^-$, which attacks organic contaminants to generate intermediates or final degradation products. The other is the reserved holes on $SnWO_4$ VB possess sufficient oxidation ability to directly degrade organic reactants.This Z-scheme heterojunction achieves spatially effective separation of charge carriers while maintaining a strong oxidation-reduction potential for separating electrons and holes, thereby improving the overall photocatalytic degradation performance.

4.Conclusions

In this work, 2D/2D SWO/BOB heterojunction photocatalysts were synthesized by a facile two-step hydrothermal method, forming close face-to-face interfacial contact. XRD、FTIR、SEM、TEM、EDS-mapping and XPS results collectively verified the successful preparation of SWO/BOB composites with strong interfacial interaction between $SnWO_4$ and BiOBr. The photocatalytic activity of SWO/BOB composites was strongly dependent on the mass ratio of $SnWO_4$. 50SWO/BOB shows optimal activity for RhB and CIP degradation under visible light. The heterojunction extends light absorption and restrains photocarrier recombination according to optical and photoelectrochemical tests. h^+ is the primary active species and $\cdot O_2^-$ acts as secondary contributor during degradation. A direct Z-scheme mechanism is illustrated: interfacial recombination of partial carriers preserves high-potential electrons and holes for pollutant oxidation-reduction. This study supplies insights into constructing high-efficiency bismuth-based photocatalysts for organic wastewater treatment.

Acknowledgements

This work was supported by the Key Scientific and Technological Research Project of Henan Province (No.232102230096), the Postgraduate Education Reform and Quality Improvement Project of Henan Province (No.YJS2025GZZ53), the Doctoral Research Startup Fund of Xinxiang University (No.1366020194), the

Horizontal Research Project (No.13440125074) and the Science and Technology Innovation Project of Xinxiang University (No.1355150129).

References

[1] S.S. Emmanuel, G.O. Achurefe, S.O. Amusat, A.A. Adesibikan, E.A. Elimian, S. Dube, M. Muzi, M.O. Idris, A comprehensive review on graphene-/graphitic carbon nitride-based MOFs for the photocatalytic purification of dye wastewater, RSC Adv. 16 (2026) 24761–24793. https://doi.org/10.1039/D6RA01722C.

[2] J. Singh, Khushboo, B. Uttam, R. Kathuria, N.K. Jaiswal, N. Tyagi, P. Kumar, A.A. Assadi, T.L.G. Hoang, P. Kumar, P. Nguyen-Tri, A Comprehensive Review on Light-Driven Detoxification of Emerging Pollutants by Scalable Photocatalytic Systems, Langmuir 42 (2026) 18570–18592. https://doi.org/10.1021/acs.langmuir.6c01097.

[3] S. Gouadria, M. Saiduzzaman, Hydrothermal synthesis of Bi-based pyrochlore oxides: a review of synthesis strategies, composition, morphology and photocatalytic applications, RSC Adv. (2026) 10.1039.D6RA02116F. https://doi.org/10.1039/D6RA02116F.

[4] M.A. Bukhari, S.M.Z.S. Bukhari, M.I. Khan, Efficient photocatalytic degradation of industrial dyes using $SnWO_4$ for wastewater treatment, Mater. 8 (2025) 100578. https://doi.org/10.1016/j.nxmate.2025.100578.

[5] R. Boddepalli, T.R. Gurugubelli, P. S.V.N, V.S.B. Netheti, S. Yusub, M.R. Tamtam, R. Koutavarapu, L.S. Pidaparthy, Efficiency and mechanistic insights of photocatalytic decomposition of tetracycline and rhodamine B utilizing Z-scheme g-C_3N_4/$SnWO_4$ heterostructures under visible light irradiation, Environ. Res. 254 (2024) 119163. https://doi.org/10.1016/j.envres.2024.119163.

[6] Sp. Keerthana, R. Yuvakkumar, G. Ravi, V.R. Sankar, S.A. Metha, S. Sagadevan, Efficient photocatalytic degradation of organic pollutants using α-$SnWO_4$ with g-C_3N_4 nanocomposites for wastewater remediation, Chemosphere 368 (2024) 143691. https://doi.org/10.1016/j.chemosphere.2024.143691.

[7] F. Imtiaz, J. Rashid, M. Xu, Hierarchically assembled $Bi_4O_5I_2$@Bi_2O_2Se/$SnWO_4$ nanosheet heterostructure for enhanced photocatalytic removal of Levofloxacin and Ibuprofen from water, J. Environ. Manage. 401 (2026) 128855. https://doi.org/10.1016/j.jenvman.2026.128855.

[8] G. Gnanamoorthy, Y. Guo, S. Magesh, S. Munusamy, V.K. Yadav, Z. Lu, Tailored $SnWO_4$/CuNiS/C Nanostructures for Integrated Photocatalytic, Antibacterial, and H29 Anticancer Activity, J. Inorg. Organomet. Polym. Mater. 36 (2026) 2424–2443. https://doi.org/10.1007/s10904-025-04039-1.

[9] Y.J. Lai, D.J. Lee, Pollutant degradation with mediator Z-scheme heterojunction photocatalyst in water: A review, Chemosphere 282 (2021) 131059.

[10] X. Fu, H. Huang, G. Tang, J. Zhang, J. Sheng, H. Tang, Recent advances in g-C_3N_4-based direct Z-scheme photocatalysts for environmental and energy applications, Chin. J. Struct. Chem. 43 (2024) 100214.

[11] S. Wang, W. Hao, Z. Liu, X. Niu, L. Wang, Q. Zhao, Two-Dimensional Direct Z-Scheme Heterojunction Photocatalysts for Highly Efficient Energy Conversion and Chemical Synthesis, ACS Nano 20 (2026) 137–162.

[12] S. Wang, P. Yang, X. Zhang, Z-scheme B-g-C_3N_4/$SnWO_4$ heterojunctions towards enhanced

photocatalytic 2,4-dichlorophenol degradation and water splitting, Int. J. Hydrog. Energy 179 (2025) 151687. https://doi.org/10.1016/j.ijhydene.2025.151687.
[13] H.C. Sathisha, Anitha, G. Krishnamurthy, R. Harini, G. Nagaraju, Hydrothermal synthesis of α-$SnWO_4$ nanoflakes for superior visible light photocatalytic and photoluminescence performance, J. Indian Chem. Soc. 102 (2025) 101743. https://doi.org/10.1016/j.jics.2025.101743.
[14] S.W. Hwang, J. S. Park, I.S. Cho, Solution Synthesis of Defect-Minimized and Visible-Light-Active Tin Tungstate (α-$SnWO_4$) Nanosheets for Enhanced Photocatalytic and Photoelectrochemical Activities, Cryst. Growth Des. 25 (2025) 4916–4923. https://doi.org/10.1021/acs.cgd.5c00412.
[15] M. Shkir, S.H. Aldirham, S. AlFaify, A.M. Ali, A novel BiOBr/rGO photocatalysts for degradation of organic and antibiotic pollutants under visible light irradiation: Tetracycline degradation pathways, kinetics, and mechanism insight, Chemosphere 357 (2024) 141934. https://doi.org/10.1016/j.chemosphere.2024.141934.
[16] Y. Peng, J. Lin, J.-L. Niu, X. Guo, Y. Chen, T. Hu, J. Cheng, Y. Hu, Synergistic Effect of Ion Doping and Type-II Heterojunction Construction and Ciprofloxacin Degradation by MIL-68(In,Bi)-NH_2 @BiOBr under Visible Light, ACS Appl. Mater. Interfaces 16 (2024) 2351–2364. https://doi.org/10.1021/acsami.3c16037.
[17] L. Ai, L. Feng, L. Wang, Y. Li, C. Tan, M. Zha, D. Jia, N. Guo, S-scheme Bi_2MoO_6/BiOBr heterostructure for effective removal of dye: Synergistic mechanism insight of adsorption-photocatalysis, Environ. Res. 275 (2025) 121301. https://doi.org/10.1016/j.envres.2025.121301.
[18] R. Sun, Z. Zhu, N. Tian, Y. Zhang, H. Huang, Hydrogen Bonds and In situ Photoinduced Metallic Bi^0 /Ni^0 Accelerating Z-Scheme Charge Transfer of BiOBr@NiFe-LDH for Highly Efficient Photocatalysis, Angew. Chem. 136 (2024) e202408862. https://doi.org/10.1002/ange.202408862.
[19] T. Liu, K. Hu, Y. Li, Y. Wang, D. Han, Z. Wang, F. Gu, The Z-Scheme MIL-88B(Fe)/BiOBr Heterojunction Promotes Fe(III)/Fe(II) Cycling and Photocatalytic-Fenton-Like Synergistically Enhances the Degradation of Ciprofloxacin, Small 20 (2024) 2309541. https://doi.org/10.1002/smll.202309541.
[20] Shashikant, R.K. Dutta, A mechanistic study on enhanced solar photocatalytic activity of $SnWO_4$/$BiMoO_6$ nanocomposites for degradation of tetracycline, Inorg. Chem. Commun. 158 (2023) 111576. https://doi.org/10.1016/j.inoche.2023.111576.
[21] S. Li, K. Dong, M. Cai, X. Li, X. Chen, A plasmonic S-scheme Au/MIL-101(Fe)/BiOBr photocatalyst for efficient synchronous decontamination of Cr(VI) and norfloxacin antibiotic, eScience 4 (2024) 100208. https://doi.org/10.1016/j.esci.2023.100208.
[22] N. Ma, S. Ma, J. Guo, G. Fan, P. Ni, Y. Wang, J. Zhu, H. Wang, Enhanced triethylamine sensing with novel WO_3 composite SnWO4 nanorod-based gas sensor, Surf. Interfaces 58 (2025) 105870. https://doi.org/10.1016/j.surfin.2025.105870.
[23] S. Li, C. Wang, K. Dong, P. Zhang, X. Chen, X. Li, MIL-101(Fe)/BiOBr S-scheme photocatalyst for promoting photocatalytic abatement of Cr(VI) and enrofloxacin antibiotic: Performance and mechanism, Chin. J. Catal. 51 (2023) 101–112. https://doi.org/10.1016/S1872-2067(23)64479-1.
[24] Shashikant, R.K. Dutta, A mechanistic study on enhanced solar photocatalytic activity of

$SnWO_4/BiMoO_6$ nanocomposites for degradation of tetracycline, Inorg. Chem. Commun. 158 (2023) 111576. https://doi.org/10.1016/j.inoche.2023.111576.

[25] J. Sun, L. Wang, T. Huang, K. Liu, T. Fu, Z. Xu, W. Yang, Z. Tong, H. Zhang, Floating $BiOBr/Ti_3C_2$ aerogel spheres for efficient degradation of quinolone antibiotics: Rapid oxygen transfer via triphase interface and effective charges separation by internal electric field, J. Colloid Interface Sci. 685 (2025) 813–825. https://doi.org/10.1016/j.jcis.2025.01.187.

[26] N. Sreeram, V. Aruna, R. Koutavarapu, D.Y. Lee, M.C. Rao, J. Shim, Fabrication of $InVO_4/SnWO_4$ heterostructured photocatalyst for efficient photocatalytic degradation of tetracycline under visible light, Environ. Res. 220 (2023) 115191. https://doi.org/10.1016/j.envres.2022.115191.

[27] X. Zhou, Y. Liu, Y. Miao, W. He, Y. Pan, A. Jing Li, J. Qin, H. Li, R. Yin, R. Qiu, Coupled radical and nonradical activation of peroxymonosulfate by the piezo-photocatalytic effect of α-$SnWO_4$/ZnO heterojunction to boost the degradation and detoxification of carbamazepine, Sep. Purif. Technol. 323 (2023) 124410. https://doi.org/10.1016/j.seppur.2023.124410.

[28] Q. Wei, S. Xiong, W. Li, C. Jin, Y. Chen, L. Hou, Z. Wu, Z. Pan, Q. He, Y. Wang, D. Tang, Double Z-scheme system of α-$SnWO_4$/UiO-66(NH_2)/g-C_3N_4 ternary heterojunction with enhanced photocatalytic performance for ibuprofen degradation and H_2 evolution, J. Alloys Compd. 885 (2021) 160984. https://doi.org/10.1016/j.jallcom.2021.160984.

[29] P. Gao, D.D. Sun, A comprehensive study of influences of sulfonated graphene sheets and CdS nanoparticles on the photocatalytic degradation and hydrogen evolution activities of TiO_2 nanospheres, Phys. Chem. Chem. Phys. (2026) 10.1039.D6CP00405A. https://doi.org/10.1039/D6CP00405A.

[30] H. Ding, Z. Qiu, Z. Qian, H. Zhang, Z. Chen, X. Xiao, Construction of a $La_2Ti_2O_7/Bi_2O_2 CO_3$ S-scheme heterojunction for efficient photocatalytic degradation of Rhodamine B, New J. Chem. (2026) 10.1039.D6NJ02206E. https://doi.org/10.1039/D6NJ02206E.

[31] S. Yaseen, M. Yaseen, T. Wang, X. Qiu, Dual Pathways Triggered by Z-Scheme Charge Separation in $ZnIn_2S_4$/Sn-Thiolate MOF for Photocatalytic H_2O_2 Generation, J. Mater. Chem. A (2026) 10.1039.D6TA05919H. https://doi.org/10.1039/D6TA05919H.

[32] J. Niu, X. Wang, J. Wang, X. Yu, H. Wei, Efficient organic pollutant photodegradation driven by sulfur-doped carbon nitride/bismuth oxybromide heterojunctions featuring enhanced interfacial charge separation, Nanoscale (2026) 10.1039.D6NR01807F. https://doi.org/10.1039/D6NR01807F.

[33] L. Yang, J. Huang, L. Shi, L. Cao, W. Zhou, K. Chang, X. Meng, G. Liu, Y. Jie, J. Ye, Efficient hydrogen evolution over Sb doped SnO_2 photocatalyst sensitized by Eosin Y under visible light irradiation, Nano Energy 36 (2017) 331–340. https://doi.org/10.1016/j.nanoen.2017.04.039.

[34] B. Sumithra, V. Saravanan, C. Ramalingan, P. Lakshmanan, D. Sivaganesh, B. Chutia, P. Bharali, A. John, R.D. Pyarasani, G. Thrimurthulu, D. Geetha, Interface engineered 2D-2D-g-$C_3N_4/SnWO_4$ S-scheme heterojunction: Clioquinol degradation and dopamine sensing properties, Inorg. Chem. Commun. 161 (2024) 112039. https://doi.org/10.1016/j.inoche.2024.112039.

[35] W. Guangchao, X. Wenhao, Z. Lanyue, M. Kang, L. Canhua, A novel sodium alginate-modified manganese–iron nodule composite for the removal of ciprofloxacin: performance and mechanism, New J. Chem. 50 (2026) 12907–12919.

https://doi.org/10.1039/D6NJ01637E.
[36] B.M. Al-howri, S. Ismail, M. Khajavian, comprehensive review of ciprofloxacin pollution in water: sources, environmental impacts, remediation techniques, and research challenges, Environ. Monit. Assess. 197 (2025) 1095. https://doi.org/10.1007/s10661-025-14454-z.
[37] Z. Zhao, W. Zhang, Y. Sun, J. Yu, Y. Zhang, H. Wang, F. Dong, Z. Wu, Bi Cocatalyst/Bi_2MoO_6 Microspheres Nanohybrid with SPR-Promoted Visible-Light Photocatalysis, J. Phys. Chem. C 120 (2016) 11889–11898. https://doi.org/10.1021/acs.jpcc.6b01188.
[38] P. Makuła, M. Pacia, W. Macyk, How To Correctly Determine the Band Gap Energy of Modified Semiconductor Photocatalysts Based on UV–Vis Spectra, J. Phys. Chem. Lett. 9 (2018) 6814–6817. https://doi.org/10.1021/acs.jpclett.8b02892.
[39] C. Yu, P. Yang, L. Tie, S. Yang, S. Dong, J. Sun, J. Sun, One-pot fabrication of β-Bi_2O_3@Bi_2S_3 hierarchical hollow spheres with advanced sunlight photocatalytic RhB oxidation and Cr(VI) reduction activities, Appl. Surf. Sci. 455 (2018) 8–17. https://doi.org/10.1016/j.apsusc.2018.04.201.
[40] G. He, J. Li, W. Qiu, L. Chen, K. Wang, Y. Liu, M. Liu, W. Li, Engineering surficial atom arrangement on α-$SnWO_4$ film for efficient photoelectrochemical water splitting, Chem. Eng. J. 469 (2023) 144096. https://doi.org/10.1016/j.cej.2023.144096.
[41] Q. Tang, Y. Wan, Z. Pan, Q. Cheng, Visible light-driven triazine-based S-scheme COF-TpTt@BiOBr heterojunction with oxygen vacancy for enhanced photocatalytic pollutants removal and hydrogen production, Environ. Res. 269 (2025) 120901. https://doi.org/10.1016/j.envres.2025.120901.
[42] S. Cao, B. Shen, T. Tong, J. Fu, J. Yu, 2D/2D Heterojunction of Ultrathin MXene/Bi_2WO_6 Nanosheets for Improved Photocatalytic CO_2 Reduction, Adv. Funct. Mater. 28 (2018) 1800136. https://doi.org/10.1002/adfm.201800136.
[43] Q. Liu, J. Shen, X. Yu, X. Yang, W. Liu, J. Yang, H. Tang, H. Xu, H. Li, Y. Li, J. Xu, Unveiling the origin of boosted photocatalytic hydrogen evolution in simultaneously (S, P, O)-Codoped and exfoliated ultrathin g-C_3N_4 nanosheets, Appl. Catal. B Environ. 248 (2019) 84–94. https://doi.org/10.1016/j.apcatb.2019.02.020.
[44] Y. Wu, Z. Liu, Y. Li, J. Chen, X. Zhu, P. Na, Construction of 2D-2D TiO_2 nanosheet/layered WS_2 heterojunctions with enhanced visible-light-responsive photocatalytic activity, Chin. J. Catal. 40 (2019) 60–69. https://doi.org/10.1016/S1872-2067(18)63170-5.
[45] Y. Luo, B. Deng, Y. Pu, A. Liu, J. Wang, K. Ma, F. Gao, B. Gao, W. Zou, L. Dong, Interfacial coupling effects in g-C_3N_4/$SrTiO_3$ nanocomposites with enhanced H2 evolution under visible light irradiation, Appl. Catal. B Environ. 247 (2019) 1–9. https://doi.org/10.1016/j.apcatb.2019.01.089.
[46] X. Wang, W. Gao, Z. Zhao, L. Zhao, J.P. Claverie, X. Zhang, J. Wang, H. Liu, Y. Sang, Efficient photo-electrochemical water splitting based on hematite nanorods doped with phosphorus, Appl. Catal. B Environ. 248 (2019) 388–393. https://doi.org/10.1016/j.apcatb.2019.02.048.
[47] M. Zhang, Z. Chen, Y. Wang, J. Zhang, X. Zheng, D. Rao, X. Han, C. Zhong, W. Hu, Y. Deng, Enhanced light harvesting and electron-hole separation for efficient photocatalytic hydrogen evolution over Cu_7S_4-enwrapped Cu_2O nanocubes, Appl. Catal. B Environ. 246 (2019) 202–210. https://doi.org/10.1016/j.apcatb.2019.01.042.
[48] Y. Zhao, Y. Wang, X. Liang, H. Shi, C. Wang, J. Fan, X. Hu, E. Liu, Enhanced photocatalytic

activity of Ag-$CsPbBr_3$/CN composite for broad spectrum photocatalytic degradation of cephalosporin antibiotics 7-ACA, Appl. Catal. B Environ. 247 (2019) 57–69. https://doi.org/10.1016/j.apcatb.2019.01.090.

[49] Z. Zhao, W. Zhang, Y. Sun, J. Yu, Y. Zhang, H. Wang, F. Dong, Z. Wu, Bi Cocatalyst/Bi_2MoO_6 Microspheres Nanohybrid with SPR-Promoted Visible-Light Photocatalysis, J. Phys. Chem. C 120 (2016) 11889–11898. https://doi.org/10.1021/acs.jpcc.6b01188.

[50] Z. Zhang, C. Gao, Z. Wu, W. Han, Y. Wang, W. Fu, X. Li, E. Xie, Toward efficient photoelectrochemical water-splitting by using screw-like SnO_2 nanostructures as photoanode after being decorated with CdS quantum dots, Nano Energy 19 (2016) 318–327. https://doi.org/10.1016/j.nanoen.2015.11.011.

[51] A. Seza, F. Soleimani, N. Naseri, M. Soltaninejad, S.M. Montazeri, S.K. Sadrnezhaad, M.R. Mohammadi, H.A. Moghadam, M. Forouzandeh, M.H. Amin, Novel microwave-assisted synthesis of porous g-C_3N_4/SnO_2 nanocomposite for solar water-splitting, Appl. Surf. Sci. 440 (2018) 153–161. https://doi.org/10.1016/j.apsusc.2018.01.133.

[52] L. Yang, J. Huang, L. Shi, L. Cao, W. Zhou, K. Chang, X. Meng, G. Liu, Y. Jie, J. Ye, Efficient hydrogen evolution over Sb doped SnO_2 photocatalyst sensitized by Eosin Y under visible light irradiation, Nano Energy 36 (2017) 331–340. https://doi.org/10.1016/j.nanoen.2017.04.039.

[53] J. Li, T. Peng, Y. Zhang, C. Zhou, A. Zhu, Polyaniline modified SnO_2 nanoparticles for efficient photocatalytic reduction of aqueous Cr(VI) under visible light, Sep. Purif. Technol. 201 (2018) 120–129. https://doi.org/10.1016/j.seppur.2018.03.010.

[54] M. Kölbach, I.J. Pereira, K. Harbauer, P. Plate, K. Höflich, S.P. Berglund, D. Friedrich, R. Van De Krol, F.F. Abdi, Revealing the Performance-Limiting Factors in α-$SnWO_4$ Photoanodes for Solar Water Splitting, Chem. Mater. 30 (2018) 8322–8331. https://doi.org/10.1021/acs.chemmater.8b03883.

[55] Z.Z. Rao Pranab Sarker, Chenqi Zhao, Lite Zhou, Ronald L. Grimm, Muhammad N. Huda, and Pratap M., Photoelectrochemical Properties and Behavior of α-$SnWO_4$ Photoanodes Synthesized by Hydrothermal Conversion of WO_3 films, ACS Appl. Mater. Interfaces. 9 (2017) 1459–1470. https://doi.org/10.1021/acsami.6b12640.

[56] M. Kölbach, H. Hempel, K. Harbauer, M. Schleuning, A. Petsiuk, K. Höflich, V. Deinhart, D. Friedrich, R. Eichberger, F.F. Abdi, R. Van De Krol, GrainBoundaries Limit the Charge Carrier Transport in Pulsed Laser Deposited α-$SnWO_4$ Thin Film Photoabsorbers, ACS Appl. Energy Mater. 3 (2020) 4320–4330. https://doi.org/10.1021/acsaem.0c00028.

[57] L.M. Azofra, L. Cavallo, J.-M. Basset, M. Harb, Need for Rationally Designed $SnWO_4$ Photo(electro)catalysts to Overcome the Performance Limitations for O_2 and H_2 Evolution Reactions, J. Phys. Chem. C 125 (2021) 8488–8496. https://doi.org/10.1021/acs.jpcc.0c11614.

[58] H. Han, S. Kment, F. Karlicky, L. Wang, A. Naldoni, P. Schmuki, R. Zboril, Sb-Doped SnO_2 Nanorods Underlayer Effect to the α-Fe_2O_3 Nanorods Sheathed with TiO_2 for Enhanced Photoelectrochemical Water Splitting, Small 14 (2018) 1703860. https://doi.org/10.1002/smll.201703860.

[59] H. Zhuang, Y. Zhang, L. Lin, W. Xu, R. Huang, S. Chen, X. Liu, Fabricating a Ternary SnO_2/ZnO/g-C_3N_4 Composite Material to Boost Photocatalytic Performance for Degradation of Antibiotics, J. Inorg. Organomet. Polym. Mater. (2026) 1–10.

https://doi.org/10.1007/s10904-026-04485-5.
[60] H. Xu, A. Li, J. Liu, J. Wang, L. Ni, Y. Xiao, Y. Jiang, Z. Liu, Enhanced photoelectron transport with favorable interfacial contact in 2D/3D $SnIn_4S_8$ nanosheet/Bi_2MoO_6 microsphere composite triggering efficient H_2O_2 generation and MO degradation, Solid State Sci. 141 (2023) 107210. https://doi.org/10.1016/j.solidstatesciences.2023.107210.
[61] Y. Zhang, X. Yu, Z. Gong, Y. Mi, M. Liu, L. Wang, S. Zeng, Facile synthesis of g-C_3N_4 /$Bi_4O_5Br_2$ S-scheme heterojunction composite with enhanced photocatalytic performance in nitrogen fixation and contaminant degradation, Appl. Surf. Sci. 700 (2025) 163100.